Spectroscopic Characterization, Computational Investigation, and Comparisons of ECX

Spectroscopic Characterization, Computational Investigation, and Comparisons of ECX^- (E = As, P, and N; X = S and O) Anions

Gao-Lei Hou,[†] Bo Chen,*[¶] Wesley J. Transue,[§] Zheng Yang,[†] Hansjörg Grützmacher,[#] Matthias Driess,[♦] Christopher C. Cummins,*[§] Weston Thatcher Borden,*[‡] and Xue-Bin Wang*[†]

[†]Physical Sciences Division, Pacific Northwest National Laboratory, P. O. Box 999, MS K8-88, Richland, WA 99352, USA

[¶]Department of Chemistry and Chemical Biology, Baker Laboratory, Cornell University, Ithaca, NY 14853, USA

[§]Department of Chemistry, Massachusetts Institute of Technology, Cambridge, MA 02139, USA

[#]Department of Chemistry and Applied Biology, ETH-Hönggerberg, 8093 Zürich, Switzerland

[‡]Department of Chemistry and the Center for Advanced Scientific Computing and Modeling, University of North Texas, 1155 Union Circle, #305070, Denton, Texas 76203-5017

[♦] Department of Chemistry: Metalorganics and Inorganic Materials, Technische Universität Berlin, Strasse des 17. Juni 135, D-10623 Berlin, Germany

Abstract

Three newly-synthesized [Na^+(221-kryptofix)] salts containing $AsCO^-$, PCO^-, and PCS^- anions were successfully electrosprayed into the vacuum, and these three ECX^- anions were investigated by negative ion photoelectron spectroscopy (NIPES) and high resolution photoelectron imaging spectroscopy. For each ECX^- anion, a well-resolved NIPE spectrum was obtained, in which every major peak is split into a doublet. The splittings are attributed to spin-orbit coupling (SOC) in the $ECX^•$ radicals. Vibrational progressions in the NIPE spectra of ECX^- were assigned to the symmetric and antisymmetric stretching modes in $ECX^•$ radicals. The electron affinities (EAs) and SOC splittings of $ECX^•$ are determined from the NIPE spectra to be: $AsCO^•$: EA = 2.414 ± 0.002 eV, SOC splitting = 988 cm^{-1}; $PCO^•$: EA = 2.670 ± 0.005 eV, SOC splitting = 175 cm^{-1}; $PCS^•$: EA = 2.850 ± 0.005 eV, SOC splitting = 300 cm^{-1}. Calculations using the B3LYP, CASPT2, and CCSD(T) methods all predict linear geometries for both the anions and neutral radicals. The calculated EAs and SOC splittings for $ECX^•$ are in excellent agreement with the experimentally-measured values. The simulated NIPE spectra, based on the calculated Franck-Condon factors, and SOC splittings nicely reproduce all of the observed spectral peaks, thus allowing unambiguous spectral assignments. The finding that PCS has the greatest EA of the three triatomic molecules considered here is counterintuitive, based upon simple electronegativity considerations, but this finding is understandable in terms of the movement of electron density from phosphorus in the HOMO of PCO^- to sulfur in the HOMO of PCS^-. Comparisons of the EAs of PCO and PCS, with the previously measured EA values for NCO and NCS are made and discussed.

Introduction

In accord with the "double bond rule,"[1] phosphorus-carbon multiply bonded systems are typically not isolable compounds unless the reactive π bond is endowed with steric protection, as was the case for ^{t}BuC≡P,[2] the first kinetically stabilized phosphaalkyne. In contrast, salts of phosphaethynolate are isolable compounds whose electronic structure is of great interest given their exceptional stability in the absence of any steric protection for the multiple bond involving the heavier p-block element. In the present combined experimental/theoretical study we seek to elucidate in detail the electronic structure of phosphaethynolate and related anions in order to shed light upon the origins of their remarkable stability, and to serve as a guide to future efforts to design systems that might incorporate multiple bonding to heavier main-group elements, freed from the constraint of sterically demanding blocking groups.

New synthetic routes that allowed the bulk preparation and isolation of 2-phosphaethynolate PCO^- were reported in 2011 and 2013,[3,4] two decades after the first synthesis of PCOLi by Becker and co-workers in 1992.[5] PCO^- has also been synthesized metathetically from CO_2 using a niobium phosphide reagent.[6] Consequently, there has been a renewed interest in exploring PCO^- chemistry.[7-24] For example, PCO^- has been shown to be an important precursor to organophosphorus compounds,[7-10] phosphorus-containing heterocycles,[11-18] and to a versatile phosphide-transfer reagent.[19,20]

The long-sought, arsenic-containing analogue of cyanate (NCO^-), 2-arsa-ethynolate $AsCO^-$ (Scheme 1),[25,26] was successfully synthesized in 2016.[27] The availability of $AsCO^-$ makes possible controlled As^- transfer in the synthesis of arsenic heterocycles.[27,28]

Studies of the coordination chemistry of PCO^- and NCO^-, as well as of their sulfur-containing analogue, PCS^- and NCS^-, in transition-metal complexes have been conducted.[21-24] Interestingly, PCO^- prefers O-coordination to actinide metals [Th, U][21] but P-coordination to W(0) and Re,[22,23] while both NCO^- and NCS^- adopt exclusively N-coordination.[21,22] On the other hand, PCS^- shows ambidentate bonding to W(0), with P and S-coordination both having been observed.[22] It has also been found that, when coordinating to coinage metals, PCO^- can act as either an η^1 or η^2 ligand, forming Au-η^1-PCO^- but Cu-η^2-PCO^- complexes.[24]

These triatomic anions are, in fact, of fundamental interest for investigations of the multiple bonds between carbon and other main group elements and of the effects that the identities of E = P or As and X = O or S have on the electronic structures of the ECX^- anions.[25,29,30] Previous studies have proposed two main resonance structures for these ECX^- molecules, one with a formal E=C double bond and the other with an E≡C triple bond (Scheme 1).[4,27,31] The P–C distances in crystallized PCO^- and PCS^- salts were measured, respectively, to be 1.579(3) and 1.555(11) Å, indicating formal triple bond character between the P and C atoms.[4,31] However, whether this is also the case when P is replaced by As has not been determined.

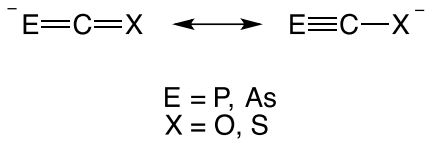

Scheme 1. Two resonance structures for ECX^- molecules, one containing an E=C double bond with the negative charge on E and the other an E≡C triple bonds with the negative charge on X.

In this article, we report a joint experimental and theoretical study on the vibronic structures and chemical bonding of three heavier analogues of cyanate anion (NCO^-) – $AsCO^-$,

PCO^-, and PCS^- – and the corresponding neutral radicals formed from the anions via electron photodetachment. The techniques employed were negative ion photoelectron spectroscopy (NIPES) and photoelectron imaging spectroscopy. DFT and high level *ab initio* electronic structure calculations were used to interpret the spectra and assign all of the peaks in them.

Well-resolved spectra, with peaks due to the transitions from the singlet ground state of ECX^- to the lowest doublet states of $ECX^{\bullet}$ were obtained for each anion, thus allowing accurate determinations of the electron affinity (EA), splitting due to spin-orbit coupling (SOC), and the vibrational frequencies of the two stretching modes in each $ECX^{\bullet}$ radical. Theoretical calculations predict linear geometries for all of the anions and neutrals investigated here, which is consistent with the absence of peaks due to E–C–X bending in the spectra. The calculated EAs, SOC splittings, and vibrational frequencies are in excellent accord with the experimental values, so that the spectra predicted by the calculations are essentially the same as those that we observed. The variations in EA between the $ECX^{\bullet}$ radicals are discussed and interpreted, based on electronegativities of the E and X atoms and the distribution of the electrons in the ECX^- HOMOs.

Experimental Methods

The NIPES experiments were performed with an apparatus consisting of an electrospray ionization source (ESI), a temperature-controlled cryogenic ion trap, and a magnetic-bottle time-of-flight (TOF) photoelectron spectrometer.[32] An acetonitrile solution of the [Na^+(221-Kryptofix)] salt of ECX^- (E = P, As; X = O, S), prepared in the glove box under an N_2 atmosphere, was used for electrospray. The ESI conditions were optimized to ensure there was a dominant mass peak for each desired ion in the respective mass spectrum.

The ions generated by ESI were guided by quadrupole ion guides into the ion trap, where they were accumulated and cooled for 20-100 ms by collisions with cold buffer gas (20% H_2 balanced in helium) at 20 K, before being transferred into the extraction zone of a TOF mass spectrometer. The cooling of the anions to 20 K improved spectral energy resolution and eliminated the possibility of the appearance of peaks in the NIPE spectra, due to hot bands.

The ECX^- ions were then mass selected, and maximally decelerated before being photodetached with 355 nm (3.496 eV) photons from a Nd:YAG laser. The laser was operated at a 20 Hz repetition rate, with the ion beam off at alternating laser shots, in order to enable shot-to-shot background subtraction. Photoelectrons were collected with ca. 100% efficiency with the magnetic bottle and analyzed in a 5.2 m long electron flight tube. The recorded TOF photoelectron spectrum was converted into an electron kinetic energy spectrum by calibration with the known NIPE spectra of I^-,[33] Br^-,[34] and phenyl thiolate (PhS^-).[35] The electron binding energy (EBE) was obtained by subtracting the electron kinetic energy from the energy of the detaching photons. The energy resolution was about 2%, i.e., ~20 meV for 1 eV kinetic energy electrons.

In addition, we also measured the high resolution photoelectron imaging spectra of $AsCO^-$ at 440 (2.821 eV) and 460 nm (2.698 eV), employing Quanta-Ray MOPO-730 OPO, pumped by Quanta-Ray PRO 270 laser, and velocity-map imaging (VMI) photoelectron spectrometer, recently developed in our lab and based on the new design of VMI electrostatic lens.[36,37] The photoelectron energy spectra were reconstructed from the accumulated images using both Maximum Entropy Velocity Image Reconstruction (MEVIR) and Maximum Entropy Velocity Legendre Reconstruction (MEVELER) methods,[38] and they gave essentially the same results.

Computational Methods

Calculations on ECX^- anions and $ECX^\bullet$ radicals were carried out with three different types of methods – the B3LYP[39,40] version of density functional theory (DFT), CASPT2,[41] which uses second-order perturbation theory to add dynamic electron correlation to complete active space (CAS)SCF wave functions, and the CCSD(T)[42,43] level of coupled-cluster theory. The all-electron aug-cc-pVTZ basis set[44,45] was employed in all three types of calculations for all of the atoms, except for the As atom in the CASPT2 calculations on $AsCO^-$ and $AsCO^\bullet$, where the aug-cc-pVTZ-PP basis set with a relativistic pseudopotential[46] (describing 1s, 2s, and 2p core electrons) was used. The aug-cc-pVTZ-PP basis set was obtained from EMSL Basis set exchange.[47,48] Natural bond orbital (NBO) analyses were performed on the ECX^- anions using NBO6 and the B3LYP methodology.[49]

B3LYP and CCSD(T) calculations, including geometry optimizations and harmonic vibrational analyses, were performed using the Gaussian 09 suite of programs.[50] CASPT2 calculations, geometry optimizations, and harmonic vibrational analyses were carried out with the Molcas program (version 8).[51]

An (8/6) active space was used in the CASSCF calculations on the ECX^- anions. The (8/6) active space consisted of 8 electrons, distributed among 6 valence π MOs. The 6 π MOs were the two degenerate pairs of the bonding, non-bonding, and antibonding π MOs in these linear molecules. The two sets of bonding and non-bonding π MOs are fully occupied in the lowest energy electronic configurations of the ECX^- anions. In the $ECX^\bullet$ radicals, one electron is removed from one of the non-bonding π MOs, leading to a (7/6) active space. The (8/6)- and (7/6)-CASSCF calculations provided the reference wave functions for the subsequent CASPT2 calculations.

Splittings due to SOC were calculated with the Molpro program (version 2010),[52] by

setting up and diagonalizing spin-orbit matrices between non-interacting, spin-orbit-free basis states. The spin-orbit-free basis states were obtained by performing multireference configuration interaction (MRCI) calculations with CASSCF reference wave functions. In the case of $ECX^{\bullet}$, the lowest degenerate pair of the $^2\Pi$ states was used for the spin-orbit-free basis states. The full valence (15/12) active space and the Douglas-Kroll contracted cc-pVTZ-DK basis set[53] were used in spin-orbit coupling calculations.

The Franck-Condon factors (FCFs) that were necessary in order to simulate the vibrational progressions in the NIPE spectra of the ECX^- anions were computed with the ezSpectrum program.[54] The optimized geometries and unscaled vibrational frequencies, computed at the B3LYP, CASPT2, and CCSD(T) levels of theory, were used as input to the ezSpectrum program for predicting the vibrational structures in NIPE spectra at these three different levels of theory. The adiabatic electron affinity (EA) of each $ECX^{\bullet}$ radical was calculated as the energy difference between the neutral and anion at their respective optimized geometries, including the zero-point energy corrections.

Experimental results

Figure 1 presents the 20 K NIPE spectra of ECX^- measured at 355 nm. Sharp and well-resolved peaks are seen in each spectrum. The 0-0 peak appears at increasing EBE on going from $AsCO^-$ to PCO^- and to PCS^-.

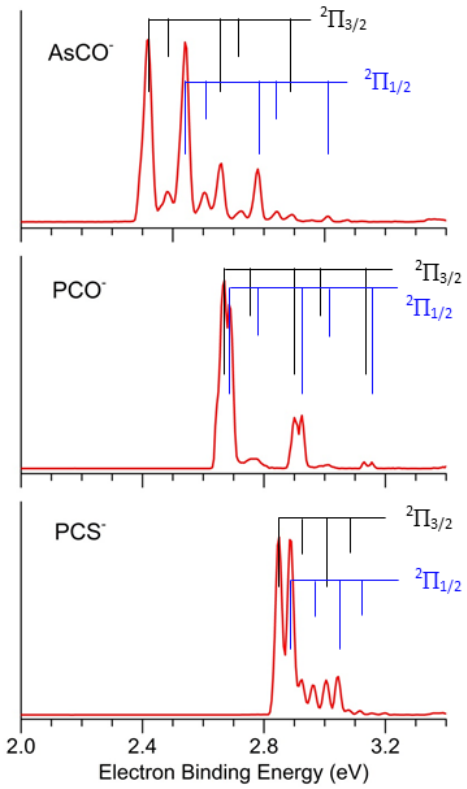

Figure 1. 20 K NIPE spectra of $AsCO^-$, PCO^-, and PCS^- at 355 nm.

The spectrum of PCO^- is relatively simple and shows two sets of short progressions, one with a spacing of 1895 ± 20 cm^{-1}, and the other with a spacing of 725 ± 20 cm^{-1}. Interestingly, the 0-0 peak and the two peaks associated with the major vibrational progression are each split into a doublet with similar intensity. As discussed in the next section, the splitting is attributed to the spin-orbit coupling (SOC) in the degenerate $^2\Pi$ states of the $PCO^•$ radical. The splittings measured in each of the three doublets are nearly identical, yielding an average value of 0.022 eV (175 cm^{-1}) for the SOC in $PCO^•$. The adiabatic detachment energy (ADE) of PCO^-, (i.e., the EA of $PCO^•$), determined from the 0–0 transition with the lowest EBE, is 2.670 ± 0.005 eV (Table 1).

The spectrum of PCS^- at 355 nm is also well resolved, exhibiting two major peaks with equal intensity at EBE ~ 2.85 eV, followed by four weak peaks spanning EBEs from 2.9 to 3.1 eV. As in the PCO^- spectrum, these peaks are assigned as being derived from two sets of short vibrational progressions, from the singlet ground state of PCS^- to the two components (Ω = 3/2 and 1/2) of the $^2\Pi$ ground state of $PCS^{\bullet}$. The SOC splitting in $PCS^{\bullet}$, determined from the spacing between the two strongest peaks in the NIPE spectrum of PCS^-, is 300 cm^{-1}, a value that is 70% larger than the splitting due to SOC in $PCO^{\bullet}$. As discussed in the next section, the larger splitting, due to SOC in $PCS^{\bullet}$ than in $PCO^{\bullet}$, is expected, because S is heavier than O. The vibrational frequencies in $PCS^{\bullet}$ are measured to be 605 and 1250 cm^{-1}. The ADE of PCS^-, measured from the first resolved strong peak, is 2.850 ± 0.005 eV, 0.18 eV higher than that of PCO^- (Table 1).

The 355 nm $AsCO^-$ spectrum is the best resolved among the three ECX^- spectra obtained in this research. Similar to the cases of PCO^- and PCS^-, all of the peaks in the NIPE spectrum of $AsCO^-$ can be arranged into pairs of doublets (indicated by blue and black lines in Figure 1), separated by the splitting due to SOC in $AsCO^{\bullet}$. Each set of peaks consists of vibrational progressions due to transitions from the ground state of $AsCO^-$ to the Ω = 3/2 and 1/2 components of the $^2\Pi$ ground state of $AsCO^{\bullet}$.

In addition to the NIPE spectrum, we also obtained the 20 K high resolution photoelectron imaging spectrum of $AsCO^-$, which was measured at 460 nm (Figure 2). (See the Supporting Information Figures S1 and S2 for the 440 nm spectra of $AsCO^-$, obtained from magnetic-bottle and velocity-map imaging photoelectron spectrometers). With the imaging technique, the resolution of the spectrum has been substantially improved and the spectral features can be completely resolved.

The experimentally measured spin-orbit splitting in AsCO• is 988 cm^{-1}, which is significantly larger than the splitting due to SOC in both PCO• and PCS•. The vibrational frequencies (525 and 1935 cm^{-1}), and EA (2.414 ± 0.002 eV) of AsCO• are given in Table 1. It is worth noting that the EA of three ECX• species increases in the order of AsCO• (2.414 eV) < PCO• (2.670 eV) < PCS• (2.850 eV), but all are substantially smaller compared to the EAs of their lighter congeners NCO• (3.609 ± 0.005 eV) and NCS• (3.537 ± 0.005 eV).[55] This may, at least partially, be attributed to the decreasing electronegativity in the order of O > N > S > P > As. However, the EA value for PCS• is greater than that of PCO•, which is the opposite of what would have been expected on the basis of the electronegativity of O being greater than that of S.

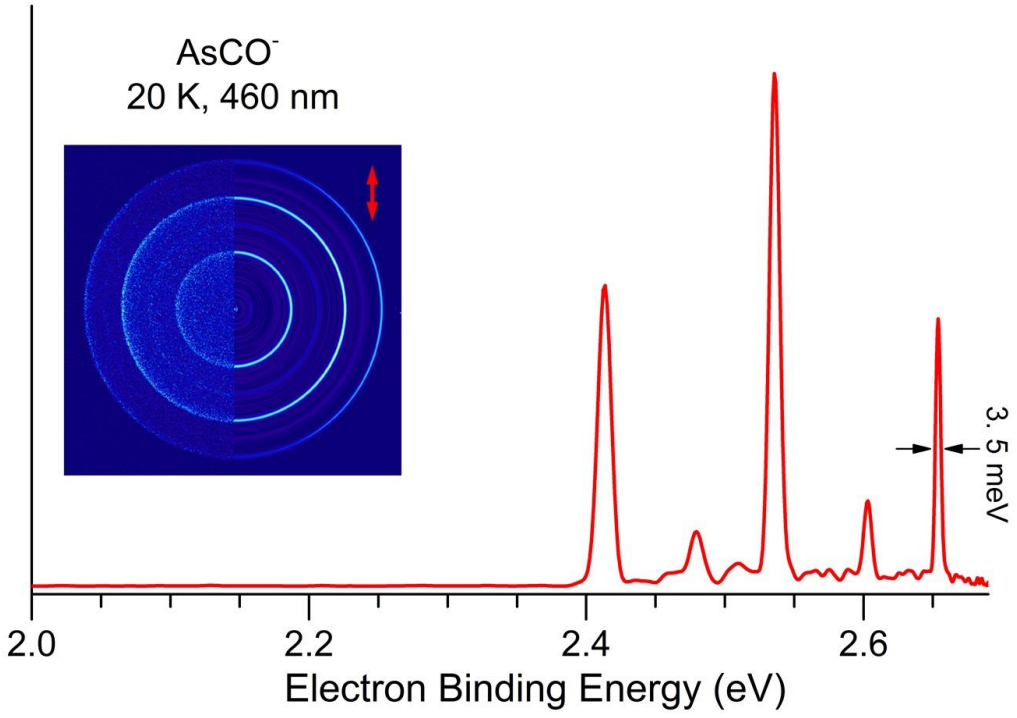

Figure 2. Photoelectron imaging spectroscopy of $AsCO^-$ at 460 nm (2.698 eV). The left part of the inserted image shows the raw image, the right part is after inverse-Abel transformation (MEVELER), and the arrow indicates the polarization of the laser.

Table 1. Comparison of the Measured and Calculated Electron Affinities (EAs), Spin-Orbit (SO) Splittings, and Vibrational Frequencies of the Two Stretching Modes in ECX•.

ECX•	EA (eV)		SOC splitting (cm^{-1})		Frequency (cm^{-1})	
	Expt.	Calc.	Expt.	Calc. [e]	Expt.	Calc.[i]
PCO•	2.670(5)	2.61 [a] 2.72 [b] 2.61 (2.61) [c]	175 ± 20	187	725 ± 20 1895 ± 20	724.7 1977
PCS•	2.850(5)	2.87 [a] 2.85 [b] 2.77 (2.76) [c]	300 ± 20	287	605 ± 20 1250 ± 20	630.0 1288.6
AsCO•	2.414(2)	2.46 [a] 2.56 [b,d] 2.44 (2.44) [c]	988 ± 10	935	525 ± 10 1935 ± 10	554.3 1979.7
NCO•	3.609[f]	3.44 [a] 3.68 [b] 3.54 (3.52) [c]	95.6 [g]	89.7		
NCS•	3.537[f]	3.50 [a] 3.50 [b] 3.49 (3.47) [c]	323.4 [h]	305		

[a](U)CCSD(T)/aug-cc-pVTZ EAs. [b](8/6)CASPT2/aug-cc-pVTZ EAs. [c](U)B3LYP/aug-cc-pVTZ EAs, with zero-point energy-corrected values in parenthesis. [d]The aug-cc-pVTZ-PP basis set with pseudopotential is used for As in CASPT2 calculation. [e]The cc-pVTZ-DK basis set and a (15/12) active space were used, and the lowest degenerate pair of $^2\Pi$ states were included in the calculation. [f]ref. 55. [g]refs. 55 and 56. [h]refs. 55 and 57. [i]Calculated at (U)CCSD(T)/aug-cc-pVTZ level of theory.

Computational Results and Discussion

Calculated Geometries. The ECX^- anions and the ECX• radicals are both calculated to be linear with all three methods – B3LYP, CASPT2, and CCSD(T). The calculated geometries of

ECX^- and $ECX^{\bullet}$ are given in Table 2. The agreement between three methods are good, except for $AsCO^{\bullet}$, where the CASPT2 As–C distance is shorter by 0.04 Å than the CCSD(T) and UB3LYP values.

Using the natural resonance theory (NRT) subroutine of natural bond orbital (NBO) methods,[49] the dominant natural Lewis structures for these anions were determined as shown in Figure 3. In each cyanate analog, ECX^-, the pnictoethynolate Lewis structure was found to have the highest weight. However, the importance of the structure with the pnictogen-carbon triple bond was found to decrease with the increasing period of E (N > P > As), but to increase with the increasing period of X (O < S). The importance of the structure with the chalcogen-carbon double bond was, not surprisingly, calculated to exhibit the opposite trends, increasing with the increasing period of E (N < P < As) and decreasing with the increasing period of X (O > S).

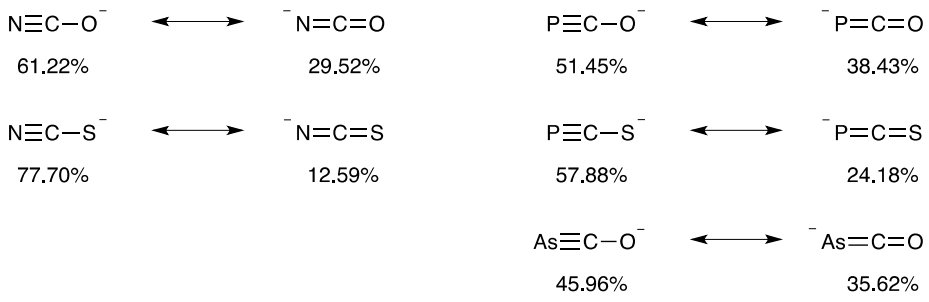

Figure 3. The natural resonance theory (NRT) weights for the dominant Lewis structures for the cyanate analogs.

The changes in the calculated E-C and C-X bond lengths in Table 2 are consistent with the expectations based on the NRT weights of the structures in Figure 3. For example, the N-C and P-C bond lengths are shorter in, respectively, NCS^- and PCS^- than in NCO^- and PCO^-; and the C-O and C-S bond lengths are longer in, respectively, NCO^- and NCS^- than in PCO^- and PCS^-.

Table 2. Bond distances in ECX^- and $ECX^{\bullet}$, calculated at (U)CCSD(T)/aug-cc-pVTZ, (8/6)CASPT2/aug-cc-pVTZ(-PP), and (U)B3LYP/aug-cc-pVTZ levels of theory.

	E–C distance (Å)			C–X distance (Å)		
	(U)CCSD(T)	CASPT2	(U)B3LYP	(U)CCSD(T)	CASPT2	(U)B3LYP
PCO^-	1.636	1.630	1.626	1.206	1.208	1.197
$PCO^{\bullet}$	1.678	1.658	1.665	1.166	1.173	1.161
PCS^-	1.608	1.610	1.598	1.642	1.626	1.630
$PCS^{\bullet}$	1.619	1.624	1.613	1.589	1.584	1.582
$AsCO^-$	1.751	1.730	1.756	1.200	1.204	1.190
$AsCO^{\bullet}$	1.801	1.759	1.804	1.163	1.170	1.156
NCO^-	1.197	1.195	1.187	1.234	1.235	1.226
$NCO^{\bullet}$	1.234	1.232	1.222	1.181	1.181	1.176
NCS^-	1.182	1.182	1.172	1.678	1.660	1.667
$NCS^{\bullet}$	1.180	1.184	1.174	1.651	1.632	1.632

The calculated E–C distances are longer and the C–X distances shorter in the radicals than in the anions, because the HOMOs of the anions, which become the SOMOs of the radicals, are slightly bonding between the E–C atoms and antibonding between the C–X atoms (Figure 4). Therefore, removal of one of the pair of electrons in each lengthens the E-C bonds and shortens the C-X bonds.

Figure 4 shows that as the period of E increases, the HOMO becomes increasingly localized on E (N < P < As). This trend is made more apparent visually by focusing on the decrease in the contribution of oxygen to the HOMO in the order E (N > P > As). The same effect, an increase in localization on X with increasing period can readily be seen in Figure 4 for

X (O < S).

These trends are confirmed numerically in Table 3, which gives the results of the NBO analysis of the compositions of the HOMOs.[49] It makes sense that in the highest energy occupied (HO)MO of an ECX^- anion, the contribution of an atom to the HOMO should increase when that atom becomes less electronegative, so that the energy of an electron on that atom rises.

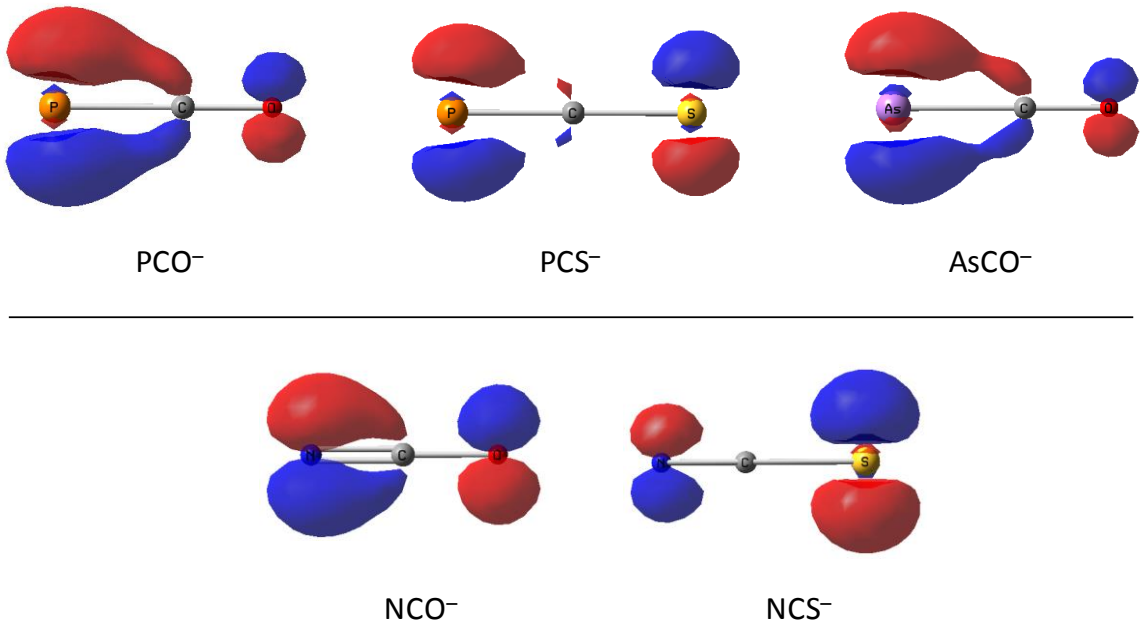

Figure 4. The HOMOs of three ECX anions, calculated at B3LYP/aug-cc-pVTZ level of theory and plotted with isovalue = 0.10. The SOMOs of $ECX^{\bullet}$ are similar in appearance.

As can be seen in Figure 4, on going from NCO^- to NCS^-, the shift of electron density onto S, makes the HOMO of the latter ion nearly nonbonding between C and both N and S. Consequently, on removal of an electron from the HOMO of NCS^-, the N-C bond length remains almost unchanged; and the C-S bond length shortens by less than 2%.

Table 3. The composition of each anion's pair of degenerate HOMOs expressed as a linear combination of natural bond orbitals (NBOs).

Anion	NBO Composition of Each Canonical HOMO
NCO^-	$0.749\ \pi_{NC} - 0.232\ \pi^*_{NC} - 0.619\ LP_O$
NCS^-	$0.408\ \pi_{NC} - 0.280\ \pi^*_{NC} - 0.867\ LP_S$
PCO^-	$0.880\ \pi_{PC} - 0.000\ \pi^*_{PC} - 0.428\ LP_O$
PCS^-	$0.672\ \pi_{PC} - 0.296\ \pi^*_{PC} - 0.676\ LP_S$
$AsCO^-$	$0.903\ \pi_{AsC} - 0.000\ \pi^*_{AsC} - 0.384\ LP_O$

EA Values. Table 1 compares the measured and calculated EAs of ECX•. Besides the EAs of PCO•, AsCO•, and PCS•, which were measured in this research, we also calculated the EAs of NCO• and NCS•, which have been measured previously by Neumark and coworkers to be 3.609 and 3.537eV, respectively.[55] In general, the agreement between the measured and calculated EAs of the five molecules in Table 1 is very good, with a difference less than 0.15 eV. A recent computational paper from the Peterson group, using a CCSD(T) composite method, reported EA = 2.850 eV for PCS•,[58] which is the same as our CASPT2 calculated value and the value measured experimentally.

When comparisons are made between the EA values for pairs of ECX molecules that differ only in the identity of E or X, the molecule with the greater EA value is, in general, the member of the pair in which E or X is the more electronegative. Thus, EA (NCO•) > EA (PCO•) > EA (AsCO•), and EA (NCO•) > EA (NCS•) > (PCS•). Therefore, it is surprising that EA (PCO•) < EA (PCS•).

Figure 4 offers a possible explanation of the apparent anomaly that the EA of PCS• is larger than the EA of PCO•. The HOMO of PCO^- has a much greater contribution from P than

the HOMO of PCS^-. The shift in electron density from P in the HOMO of PCO^- to the more electronegative S atom in HOMO of PCS^- might be expected to make the latter anion more difficult to ionize than the former, as is found to be the case.

This explanation comports with the NBO analysis of the composition of each anion's HOMO in Table 3. Table 3 shows that electron density is transferred from E to X in going from NCO^- to NCS^- and from PCO^- to PCS^-. Since nitrogen's electronegativity is greater than that of sulfur, the increased contribution of the relatively electropositive sulfur lone pair in NCS^- results in a diminished EA compared to NCO^-. This effect is reversed between PCO^- and PCS^-, where sulfur's heightened electronegativity compared to phosphorus causes the increased contribution of the sulfur lone pair to raise the EA. Thus, one might expect the corresponding neutral radical of the unknown $AsCS^-$ anion to have a higher EA than that of the $AsCO^-$ anion.

Splittings Due to SOC. Table 1 compares not only the measured and calculated EAs of $ECX^{\bullet}$, but also the measured and computed splitting due to spin-orbit coupling (SOC). The calculated SOC splittings for the $ECX^{\bullet}$ molecules are within 7% of the measured values. Peterson recently reported a calculated SOC splitting of 318.7 cm^{-1} for $PCS^{\bullet}$,[58] which is 19 cm^{-1} larger than the measured splitting and 32 cm^{-1} larger than our calculated SOC splitting.

In atoms SOC increases as Z^4/n^3, where Z is the effective nuclear charge and n is the principal quantum number.[59] Therefore, heavy elements should have much larger SOCs than lighter elements in the same column of periodic table. For example, the experimentally measured spin-orbit splitting in the lowest $^2P^o$ term of an As atom is 0.057 eV = 461 cm^{-1}, but for a P atom the splitting is only 0.003 eV = 26 cm^{-1}.[60] Similarly, the experimentally measured spin-orbit splitting between the J = 1/2 and 3/2 components of the $^2\Pi_g$ state of the $As_2^{\bullet-}$ diatomic anion, is 2065 cm^{-1},[61] but in $P_2^{\bullet-}$ the splitting is only161 cm^{-1}.[62,63]

In ECX• molecules, the spin-orbit coupling constants depend on not only the atomic numbers of the E and X atoms, but also on the density of the SOMOs on these atoms. Figure 4 shows that the contributions of P to the SOMO of PCO• and of As to the SOMO of AsCO• are similar. Therefore, the greater atomic number of As than of P should make the spin-orbital coupling constant much larger in AsCO• than in PCO•.

In fact, Table 1 shows this to be the case for both the measured and calculated spin-orbit splittings in these two ECX• radicals. Consequently, the much larger splitting between the doublets in the NIPE spectrum of $AsCO^-$ than that of PCO^- is qualitatively what would be expected if these doublets are due to spin-orbit coupling in the AsCO• and PCO• radicals, formed by electron photo-detachment from the anions.

Vibrational Progressions. In addition to spin-orbit coupling, vibrational progressions also contribute to the peaks in the NIPE spectra of ECX^- in Figure 1. Therefore, we calculated the Franck-Condon factors (FCFs) for the vibrational peaks in the transitions from ECX^- to ECX•. The simulated stick spectra of ECX^-, obtained using the FCFs calculated at (U)CCSD(T)/aug-cc-pVTZ level of theory, are shown in Figure 5. The FCFs computed by B3LYP and CASPT2, give simulated stick spectra that look similar to those in Figure 5.[64]

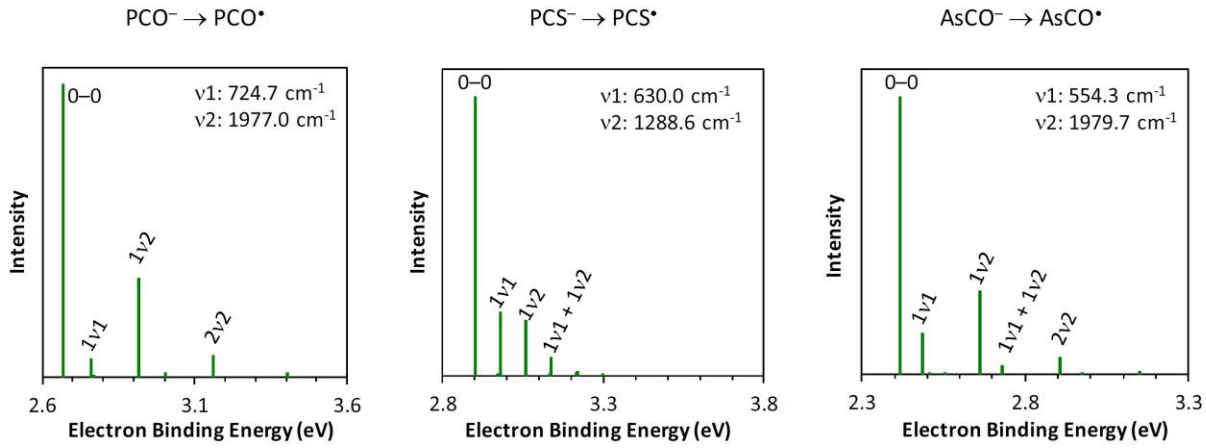

Figure 5. Simulated stick NIPE spectra of ECX^- ions, with FCFs calculated at (U)CCSD(T)/aug-cc-pVTZ level of theory. Peaks in each simulated spectrum are due to the 0-0 peak and to vibrational progressions in the "symmetric" stretching (ν1) and antisymmetric stretching (ν2) modes in the $ECX^{\bullet}$ radicals.

Since the ECX^- anions and the $ECX^{\bullet}$ radicals are all calculated to have linear geometries, bending vibrations should not contribute to the NIPE spectra. Therefore, progressions in only the symmetric and antisymmetric E–C–X stretching modes are expected to be seen. The simulations in Figure 5 show that both stretching modes are calculated to produce vibrational progressions in the $ECX^- \rightarrow ECX^{\bullet}$ transitions. The symmetric stretching mode (ν1) is calculated to have a lower frequency than the antisymmetric stretching mode (ν2), and the 0-0 peak is calculated to be the most intense peak in each of the three NIPE spectra.

In order to compare the vibrational progressions in the simulated and experimental NIPE spectra, the simulated stick spectra were convoluted, replacing each stick with a Gaussian of 25 meV full-width at half-maximum (FWHM) for $AsCO^-$ and PCS^-, and 18 meV FWHM for PCO^-. Spin-orbit splitting was included in the computed spectra by dividing each stick into a doublet, using a spacing that was equal to the experimentally observed spin-orbit splitting. As shown in Figure 6, the simulations give vibrational progressions in the calculated NIPE spectra that agree well with the vibrational progressions in the experimental spectra.

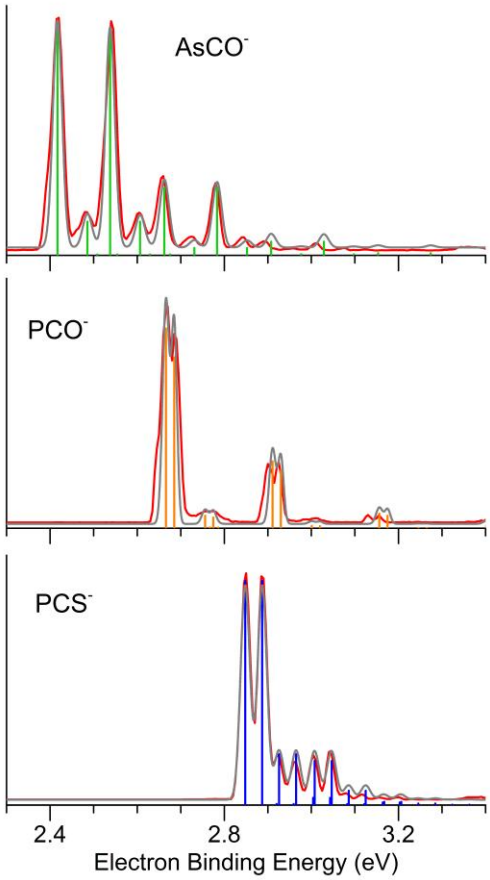

Figure 6. The vibrational peaks in the (U)CCSD(T)/aug-cc-pVTZ simulated NIPE stick spectra (green for $AsCO^-$, orange for PCO^-, and blue for PCS^-), separated by the corresponding spin-orbit splitting. Convoluted spectra were obtained by using Gaussian line shapes with 25 meV ($AsCO^-$ and PCS^-) and 18 meV (PCO^-) full widths at half maxima for each stick. The convoluted spectra (grey) are superimposed onto the experimental 355 nm NIPE spectrum (red).

Conclusions

We have carried out an experimental and computational study of the NIPE spectra of the heavy pseudohalides $AsCO^-$, PCO^-, and PCS^- – three new members of the pnictogen family of triatomic anions. In order to simulate the spectra, we have computed the geometries, electronic structures, and vibrational frequencies of these anions and of the corresponding neutral radicals.

The measurement of well-resolved NIPE spectra and the unambiguous assignments of the peaks in the spectra with the aid of electronic structure calculations, allow the EA, spin-orbit splitting, and vibrational frequencies of each $ECX^{\bullet}$ radical to be accurately determined. The measured EAs increase in the order: $AsCO^{\bullet}$ (2.414 eV) < $PCO^{\bullet}$ (2.670 eV) < $PCS^{\bullet}$ (2.850 eV); but all of these EAs are appreciably smaller than the EAs of $NCO^{\bullet}$ (3.609 eV) and $NCS^{\bullet}$ (3.537). This finding suggests that the ECX^{-} anions studied in this work might act as softer ligands than both NCO^{-} and NCS^{-}.

In addition, the calculations find greater electron density on the As and P atoms than on the O atoms in the HOMOs of $AsCO^{-}$ and PCO^{-} (and in the SOMOs of $AsCO^{\bullet}$ and $PCO^{\bullet}$), but nearly equal densities on the P and S atoms in HOMO of PCS^{-} (and in the SOMO of $PCS^{\bullet}$). This finding helps to rationalize why the EA of PCS^{-} is, unexpectedly, both calculated and found to be greater than that of PCO^{-}.

The experimental and computational results that emerge from the research described in this paper should lead to a better understanding of the electronic structures, coordination chemistries, and reactivity patterns of the newly-available ECX^{-} anions (E = P and As, X = O and S).

Associated Content

Supporting Information

The 20 K NIPE spectrum of $AsCO^{-}$ at 440 nm (2.821 eV) obtained from magnetic-bottle photoelectron spectrometer (Figure S1); The 20 K photoelectron imaging spectrum of $AsCO^{-}$ at 460 nm (2.698 eV) and 440 nm (2.821 eV) obtained from velocity-map imaging photoelectron spectrometer using MEVIR transformation method (Figure S2); Simulated stick NIPE spectra of ECS^{-} ions, with FCFs computed by B3LYP and CASPT2 methods (Figure S3); The simulated NIPE spectrum of NCO^{-} and its comparison with the experimental spectrum obtained by

Neumark and co-workers (Figure S4); Calculated spin-orbit splittings for the P and As atomic and diatomic species and their comparison with the experimentally measured values (Table S1); The effect of basis set, active space size, and inclusion of higher states on the calculated spin-orbit splitting in PCO$^{\bullet}$, AsCO$^{\bullet}$, and PCS$^{\bullet}$ (Table S2); Calculated frequencies of the symmetric and antisymmetric stretching modes (Table S3); Calculated absolute energies (Table S4); Calculated Franck-Condon factors (Table S5).

Author Information

Corresponding Authors

Bo Chen: bc336@cornell.edu

Christopher Cummins: ccummins@mit.edu

Weston T. Borden: Weston.Borden@unt.edu

Xue-Bin Wang: Xuebin.wang@pnnl.gov

Notes

The authors declare no competing financial interest

Acknowledgement. We thank Professor Tao Zeng of Carleton University for helpful discussions regarding spin-orbit calculations in our paper and Dr. Shenglai Yao of TU Berlin for the preparation of a sample of Na(OCAs). The experimental work done at PNNL was supported by U.S. Department of Energy (DOE), Office of Science, Office of Basic Energy Sciences, the Division of Chemical Sciences, Geosciences, and Biosciences, and performed using EMSL, a national scientific user facility sponsored by DOE's Office of Biological and Environmental Research and located at Pacific Northwest National Laboratory, which is operated by Battelle

Memorial Institute for the DOE. The research at the University of North Texas was supported by the Robert A. Welch Foundation (Grant B0027). The experimental work conducted at MIT was supported by the National Science Foundation under grant no. CHE-1362118.

References

(1) Knoll, R. A. F. *Adv. Inorg. Chem.* **1989**, *33*, 259.

(2) Becker, G.; Gresser, G.; Uhl, W. *Z. Naturforsch. B*, **1981**, *36*, 16.

(3) Puschmann, F. F.; Stein, D.; Heift, D.; Hendriksen, C.; Gal, Z. A.; Grützmacher, H. F.; Grützmacher, H. *Angew. Chem. Int. Ed.* **2011**, *50*, 8420.

(4) Jupp, A. R.; Goicoechea, J. M. *Angew. Chem. Int. Ed.* **2013**, *52*, 10064.

(5) Becker, G.; Schwarz, W.; Seidler, N.; Westerhausen, M. *Z. Anorg. Allg. Chem.* **1992**, *612*, 72.

(6) Krummenacher, I.; Cummins, C. C. *Polyhedron* **2012**, *32*, 10.

(7) Jupp, A. R.; Goicoechea, J. M. *J. Am. Chem. Soc.* **2013**, *135*, 19131.

(8) Geeson, M. B.; Jupp, A. R.; McGrady, J. E.; Goicoechea, J. M. *Chem. Commun.* **2014**, *50*, 12281.

(9) Jupp, A. R.; Trott, G.; Payen de la Garanderie, É.; Holl, J. D. G.; Carmichael, D.; Goicoechea, J. M. *Chem. Eur. J.* **2015**, *21*, 8015.

(10) Hinz, A.; Labbow, R.; Rennick, C.; Schulz, A.; Goicoechea, J. M. *Angew. Chem. Int. Ed.* **2017**, *56*, 3911.

(11) Robinson, T. P.; Goicoechea, J. M. *Chem. Eur. J.* **2015**, *21*, 5727.

(12) Heift, D.; Benko, Z.; Grützmacher, H. *Chem. Eur. J.* **2014**, *20*, 11326.

(13) Heift, D.; Benko, Z.; Grützmacher, H. *Angew. Chem. Int. Ed.* **2014**, *53*, 6757.

(14) Chen, X.; Alidori, S.; Puschmann, F. F.; Santiso-Quinones, G.; Benko, Z.; Li, Z.; Becker, G.; Grützmacher, H. F.; Grützmacher, H. *Angew. Chem. Int. Ed.* **2014**, *53*, 1641.

(15) Heift, D.; Benko, Z.; Grützmacher, H. *Dalton Trans.* **2014**, *43*, 831.

(16) Nakajima, K.; Liang, W.; Nishibayashi, Y. *Org. Lett.* **2016**, *18*, 5006.

(17) Suter, R.; Mei, Y.; Baker, M.; Benkő, Z.; Li, Z.; Grützmacher, H. *Angew. Chem. Int. Ed.* **2017**, *56*, 1356.

(18) Hansmann, M. M.; Ruiz, D. A.; Liu, L. L.; Jazzar, R.; Bertrand, G. *Chem. Sci*. **2017**, DOI 10.1039/C7SC00300E.

(19) Tondreau, A. M.; Benkő, Z.; Harmer, J. R.; Grützmacher, H. *Chem. Sci*. **2014**, *5*, 1545.

(20) Heift, D.; Benkő, Z.; Grützmacher, H.; Jupp, A. R.; Goicoechea, J. M. *Chem. Sci*. **2015**, *6*, 4017.

(21) Camp, C.; Settineri, N.; Lefèvre, J.; Jupp, A. R.; Goicoechea, J. M.; Maron, L.; Arnold, J. *Chem. Sci*. **2015**, *6*, 6379.

(22) Jupp, A. R.; Geeson, M. B.; McGrady, J. E.; Goicoechea, J. M. *Eur. J. Inorg. Chem.* **2016**, *2016*, 639.

(23) Alidori, S.; Heift, D.; Santiso-Quinones, G.; Benkő, Z.; Grützmacher, H.; Caporali, M.; Gonsalvi, L.; Rossin, A.; Peruzzini, M. *Chem. Eur. J.* **2012**, *18*, 14805

(24) Liu, L.; Ruiz, D. A.; Dahcheh, F.; Bertrand, G.; Suter, R.; Tondreau, A. M.; Grützmacher, H. *Chem. Sci*. **2016**, *7*, 2335.

(25) Lu, Y.; Wang, H.; Xie, Y.; Liu, H.; Schaefer, H. F. *Inorg. Chem.* **2014**, *53*, 6252.

(26) Zhang, L.; Dong, J.; Zhou, M. *Chem. Phys. Lett.* **2001**, *335*, 334.

(27) Hinz, A.; Goicoechea, J. M. *Angew. Chem. Int. Ed.* **2016**, *55*, 8536.

(28) Hinz, A.; Goicoechea, J. M. *Angew. Chem. Int. Ed.* **2016**, 55, 15515.

(29) Pyykko, P.; Riedel, S.; Patzschke, M. *Chem. Eur. J.* **2005**, *11*, 3511.

(30) Pyykko, P.; Atsumi, M. *Chem. Eur. J.* **2009**, *15*, 12770.

(31) Becker, G.; Hübler, K. *Z. Anorg. Allg. Chem.* **1994**, *620*, 405.

(32) Wang, X.-B.; Wang, L.-S. *Rev. Sci. Instrum.* **2008**, *79*, 073108.

(33) Hanstrop, D.; Gustafsson, M. *J. Phys. B: At. Mol. Opt. Phys.* **1992**, *25*, 1773.

(34) Blondel, C.; Cacciani, P.; Delsart, C.; Trainham, R. *Phys. Rev. A* **1989**, *40*, 3698.

(35) Kim, J. B.; Yacovitch, T. I.; Hock, C.; Neumark, D. M. *Phys. Chem. Chem. Phys.*, **2011**, *13*, 17378.

(36) Weichman, M. L.; DeVine, J. A.; Levine, D. S.; Kim, J. B.; Neumark, D. M. *Proc. Natl. Acad. Sci., USA* **2016**, *113*, 1698.

(37) León, I.; Yang, Z.; Liu, H.-T.; Wang, L.-S. *Rev. Sci. Instrum.* **2014**, *85*, 083106.

(38) Dick, B. *Phys. Chem. Chem. Phys.*, **2014**, *16*, 570.

(39) Becke, A. D. *J. Chem. Phys.* **1993**, *98*, 5648.

(40) Lee, C.; Yang, W.; Parr, R. G. *Phys. Rev. B* **1988**, *37*, 785.

(41) Andersson, K.; Malmqvist, P.; Roos, B. O. *J. Chem. Phys.* **1992**, *96*, 1218.

(42) Purvis, G. D.; Bartlett, R. *J. Chem. Phys.* **1982**, *76*, 1910.

(43) Raghavachari, K.; Trucks, G. W.; Pople, J. A.; Head-Gordon, M. *Chem. Phys. Lett.* **1989**, *157*, 479.

(44) Dunning, T. H. *J. Chem. Phys.* **1989**, *90*, 1007.

(45) Kendall, R. A.; Dunning, T. H.; Harrison, R. J. *J. Chem. Phys.* **1992**, *96*, 6796.

(46) Peterson, K. A. *J. Chem. Phys.* **2003**, *119*, 11099.

(47) Feller, D. *J. Comput. Chem.* **1996**, *17*, 1571.

(48) Schuchardt, K. L.; Didier, B. T.; Elsethagen, T.; Sun, L.; Gurumoorthi, V.; Chase, J.; Li, J.;

Windus, T. L. *J. Chem. Inf. Model.* **2007**, *47*, 1045.

(49) Glendening, E. D.; Badenhoop, J. K.; Reed, A. R.; Carpenter, J. E.; Bohmann, J. A.; Morales, C. M.; Landis, C. R.; Weinhold, F. NBO 6.0 (Theoretical Chemistry Institute, University of Wisconsin, Madison, 2013.

(50) Frisch, M. J.; Trucks, G. W.; Schlegel, H. B.; Scuseria, G. E.;Robb, M. A.; Cheeseman, J. R.; Scalmani, G.; Barone, V.; Mennucci, B.; Petersson, G. A.; Nakatsuji, H.; Caricato, M.; Li, X.; Hratchian, H. P.; Izmaylov, A. F.; Bloino, J.; Zheng, G.; Sonnenberg, J. L.; Had, M.;Fox, D. J. Gaussian 09, Revision D.01. *Gaussian Inc., Wallingford*. 2013.

(51) Aquilante, F.; Autschbach, J.; Carlson, R. K.; Chibotaru, L. F.; Delcey, M. G.; De Vico, L.; Fdez. Galván, I.; Ferré, N.; Frutos, L. M.; Gagliardi, L.; Garavelli, M.; Giussani, A.; Hoyer, C. E.; Li Manni, G.; Lischka, H.; Ma, D.; Malmqvist, P. Å; Müller, T.; Nenov, A.; Olivucci, M.; Pedersen, T. B.; Peng, D.; Plasser, F.; Pritchard, B.; Reiher, M.; Rivalta, I.; Schapiro, I.; Segarra-Martí, J.; Stenrup, M.; Truhlar, D. G.; Ungur, L.; Valentini, A.; Vancoillie, S.; Veryazov, V.; Vysotskiy, V. P.; Weingart, O.; Zapata, F.; Lindh, R. *J. Comput. Chem.* **2016**, *37*, 506.

(52) (a) Werner, H.-J.; Knowles, P. J.; Knizia, G.; Manby F. R.; Schütz, M.; *WIREs Comput. Mol. Sci.* **2012**, *2*, 242. (b) Werner, H.-J.; Knowles, P. J.; Knizia, G.; Manby, F. R.; Schütz, M.; Celani, P.; Korona, T.; Lindh, R.; Mitrushenkov, A.; Rauhut, G.; Shamasundar, K. R.; Adler, T. B.; Amos, R. D.; Bernhardsson, A.; Berning, A.; Cooper, D. L.; Deegan, M. J. O.; Dobbyn, A. J.; Eckert, F.; Goll, E.; Hampel, C.; Hesselmann, A.; Hetzer, G.; Hrenar, T.; Jansen, G.; Köppl, C.; Liu, Y.; Lloyd, A. W.; Mata, R. A.; May, A. J.; McNicholas, S. J.; Meyer, W.; Mura, M. E.; Nicklass, A.; O'Neill, D. P.; Palmieri, P.; Peng, D.; Pflüger, K.; Pitzer, R.; Reiher, M.; Shiozaki, T.; Stoll, H.; Stone, A. J.;

Tarroni, R.; Thorsteinsson, T.; Wang, M. MOLPRO, version 2010.1, a package of ab initio programs, see http://www.molpro.net.

(53) de Jong, W. A.; Harrison, R. J.; Dixon, D. A. *J. Chem. Phys.* **2001**, *114*, 48.

(54) Mozhayskiy, V. A.; Krylov, A. I. ezSpectrum, version 3.0; available at http://iopenshell.usc.edu/downloads.)

(55) Bradforth, S. E.; Kim, E. H.; Arnold, D. W.; Neumark, D. M. *J. Chem. Phys.* **1993**, *98*, 800.

(56) Northrup, F. J.; Wu, M.; Sears, T. J. *J. Chem. Phys.* **1992**, *96*, 7218.

(57) Northrup, F. J.; Sears, T. J. *J. Chem. Phys.* **1989**, *91*, 762.

(58) Finney, B.; Mitrushchenkov, A. O.; Francisco, J. S.; Peterson, K. A. *J. Chem. Phys.* **2016**, *145*, 224303.

(59) The Z^4 denpendence on nuclear charge only holds for hydrogenic systems with one electron. For multi-electron atoms, the inter-electronic SOC leads to a shielding effect to the nuclear-electron SOC. The magnitude of SOC hence increases more slowly, following Z^2. See: Zeng, T.; Fedorov, D. G.; Klobukowski, M. *J. Chem. Phys.* **2011**, *134*, 024108.

(60) Sansonetti, J. E.; Martin, W. C. *J. Phys. Chem. Ref. Data* **2005**, *34*, 1559.

(61) Lippa, T. P.; Xu, S.-J.; Lyapustina, S. A.; Nilles, J. M.; Bowen, K. H. *J. Chem. Phys.* **1998**, *109*, 10727.

(62) Jones, R. O.; Ganteför, G.; Hunsicker, S.; Pieperhoff, P. *J. Chem. Phys.* **1995**, *103*, 9549.

(63) Our calculated spin-orbit splittings for these P and As atomic and diatomic species are in qualitative agreement with the experimentally measured values (Table S2).

(64) These simulated NIPE spectra are given in Figure S3 of the Supporting Information. We also simulated the NIPE spectrum of NCO^- and compared the simulated spectrum with the

experimental spectrum that was obtained by Neumark and co-workers.[55] As shown in Figure S4 of the SI, the simulated spectrum matches the experimental NIPE spectrum of NCO^- very well.

TOC Graphic